
Use of the OzDES Survey for Visualization in Supernova Cosmology

Hugh McDougall 2016/2017
Under the Supervision of Prof Tamara Davis Samuel

Hugh McDougall

This project used the Australian Dark Energy Survey (OzDes) supernova and galaxy data to develop two visualizations of cosmological phenomena: the extension of an animated 3D map of the OzDes galaxies by Hinton to include physically representative supernovae, and a 3D map of weak gravitational lensing magnification using count-density of galaxies in the DES field. The supernova was a full success, accomplishing all set goals, and the density map is practically functional, successfully reproducing many of the phenomena expected from the literature, but is subject to a number of artifacts relating to integration and imprecise measurements of density.

CONTENTS

1 Introduction	3
2 Background	3
2.1 Cosmological Expansion	3
2.2 Gravitational Lensing	4
2.3 Supernovae	5
3 Supernova Animation	6
3.1 Supernova Simulation	6
3.2 Frame Rendering.....	7
3.3 False Colour Schemes	8
4 Weak Gravitational Lensing Map.....	9
4.1 Methods.....	9
4.1.1 Model.....	10
4.1.2 Galaxy Count Method	10
4.1.3 Density Estimation	11
4.2 Results.....	12
4.2.1 Structure & Resolution.....	12
4.2.2 Magnitude & Distribution	15
5 Conclusion & Recommendations.....	17
5.1 Supernova Visualization.....	17
5.2 Density Map.....	17
5.3 Additional Visualizations.....	17
6 References	18

1 INTRODUCTION

The fundamental goal of cosmology is to understand the history and makeup of the universe at large, a goal that requires us to make measurements of events across massive distances and time scales. Core to this endeavor is the study of supernovae, specifically type Ia supernovae, one of the few types of events bright enough to observe at cosmological distances while still having consistent enough properties to make meaningful measurements from.

These measurements are subject to systematic biases that can offset them from their true values, or significantly increase their dispersion. Visualizing events and effects at this scale can be counterintuitive, and so there is a practical need to be able to create simple, easily readable displays of phenomena related to supernova cosmology.

This project focuses on two such visualizations using data from the ‘Dark Energy Survey’ for both galaxies and supernovae: the addition of a physically representative animation of DES supernovae, including their redshifts and light curves, to a 3D animation of the DES field constructed by (Hinton, 2016), and a 3D map of magnification produced by weak gravitational lensing, using density estimates based on the count-density of galaxies in the DES field. The latter of these is of practical interest, as an accurate map of magnification will allow supernova measurements to be refined by accounting for this lensing effect.

2 BACKGROUND

2.1 COSMOLOGICAL EXPANSION

Space is known to be expanding at an accelerating rate, where any given scale grows at a rate instantaneously proportional to its own length (Perlmutter & Schmidt, 2003):

$$\frac{1}{a} \frac{da}{dt} = H(t)$$

This ‘Hubble flow’ means that objects recede from us at a rate proportional to their distance:

$$v_R(t) = H(t) \cdot R(t)$$

Here, $H(t)$ is the Hubble parameter, a slowly time varying property of the universe, with a present day value of H_0 . Here, we define length scales by a unitless ‘scale factor’, the ratio of the length at some time to length at the present day:

$$R(t) = R_0 a(t)$$

This means that any unforced physical separation increases by a set factor over a given time, irrespective of that separation’s size. Beyond extremely early times, this expansion is described by a ‘Cosmological Constant, Cold Dark Matter’ (Λ CDM) model, in which the Hubble parameter evolves as a function of the scale factor:

$$\left(\frac{H(t)}{H_0}\right)^2 = \Omega_\Lambda + \Omega_k a^{-2} + \Omega_m a^{-3} + \Omega_R a^{-4}$$

Here, ‘ Ω_m, Ω_R ’ & ‘ Ω_Λ ’ are measures of the present day prevalence of matter, radiation and ‘dark energy’ in the universe, respectively. Ω_k is a term related to the curvature of space, which in turn is related to the other densities by ‘ $\Omega_k = 1 - \sum_{i \neq k} \Omega_i$ ’. Each ‘ Ω_i ’ is a ratio of that

species' energy density to the critical value that causes the curvature of the universe to be flat:

$$\Omega_i = \frac{\rho_i}{\rho_{crit}},$$

$$\rho_{crit} \equiv \frac{3H_0^2}{8\pi G} \text{ (Perlmutter \& Schmidt, 2003) \textcircled{2}}$$

For the purposes of this report, we assume the parameters to be constant, at approximate values:

$$\begin{aligned} \Omega_m &= 0.3 \\ \Omega_k &= \Omega_R = 0 \\ \Omega_\Lambda &= 0.7 \end{aligned}$$

For which the Hubble parameter is easy to calculate:

$$H(z) = H_0 \sqrt{\Omega_\Lambda + \Omega_m a^{-3}}$$

The expansion of the universe produces a 'cosmological redshift' of light as it travels:

$$z \equiv \frac{\Delta\lambda}{\lambda} = \frac{1}{a} - 1$$

Expansion is 1-dimensional, a given time corresponds to a set redshift and scale factor, and so this easily measurable property can be used to describe the age and distance of an event or object in the Hubble flow.

This allows for the calculation of the 'comoving distance', χ , which describes the separation of events in a way that doesn't change with expansion, and is required to the calculation of gravitational lensing:

$$\chi(z) = \int_0^z \frac{c}{H(z)} dz \text{ (Taylor, 2016)}$$

2.2 GRAVITATIONAL LENSING

Though the density of the universe is constant at large enough scales (>100 Mpc) (Wojtak, Davis, & Jophiel, 2015), there are still significant fluctuations in density on a number of length

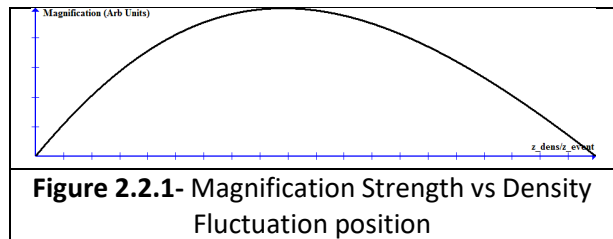
scales. These overdense and underdense regions warp space, causing the paths of light passing through them to converge (magnifying) and diverge (demagnifying) respectively.

This is referred to as 'weak lensing' (in contrast to strong lensing, which creates more complicated lensing effects), and is one of the focuses of this report. This distortion does not affect the average of the distribution of observed brightnesses, only its shape, creating a long 'tail' of rare strongly magnified events as compared to more common weak demagnification events (Perlmutter & Schmidt, 2003). The magnification due to weak lensing is given by an integral over the comoving distance:

$$\delta m_i = \frac{-5}{\ln|10|} \cdot \frac{3H_0^2 \Omega_m}{2c^2} \int_0^{\chi_i} \chi \frac{\chi_i - \chi}{\chi_i} \frac{\delta(\chi)}{a(\chi)} d\chi$$

(Taylor, 2016)

One result of this is equation that density fluctuations roughly halfway between the event and the observer have the strongest impact on the lensing (figure 2.2.2)



2.3 SUPERNOVAE

One of the best markers we have for measurements on the cosmological scale are supernovae: extremely luminous events occurring sporadically throughout the sky, mostly in galaxies, that we now know to be various processes marking the death of massive stars or binary pairs. Supernovae are classified by their observable properties: type-I supernovae are those that do not produce hydrogen spectral lines, while type-II are those that do. Of the type-I's, those with silicon spectral lines are type-Ia, while those without are either Ib or Ic.

Type I supernovae are those with hydrogen lines in their spectra, but the class actually includes two distinct phenomena. Type Ia supernovae, which produce silicon lines, are created by the core-detonation of a white dwarf due to mass sharing with its partner in a binary pair. Type Ib and Ic, meanwhile, are core collapse of stars that have already shed their hydrogen shells, and do not demonstrate silicon lines (Perlmutter & Schmidt, 2003).

Type I supernovae form the best 'standard candles' in modern astronomy, with remarkably consistent peak brightnesses ($\sigma = 0.6$ magnitudes) across all events irrespective of environment or progenitor event even when failing to distinguish between a, b and c. When only type Ia are considered, eliminating peculiar cases, the dispersion drops even further to $\sigma = 0.25$ magnitudes, and this variance can be refined even further by splitting the supernovae into increasingly finer categories and accounting for external sources of variation or systematic error.

In addition to their consistent brightness, type Ia's have well characterized 'light curves'

describing the relative luminosity of different colours at different times. In the rest frame (i.e. in the absence of redshift) supernovae are predominantly 'white' in visual bands, and take about 25 days from the start of the event to reach peak brightness, with brightness trailing off for another few weeks, though this timescale can lengthen or shorten based on the property of 'stretch'.

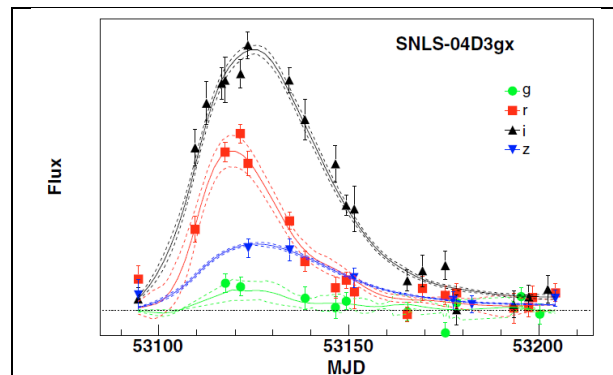


Fig 2.3.1-Measured Supernova Light Curve & Model (Guy, Astier, & Baumont, 2007)

Without a precise theory for simulating the properties of all supernovae, relationships between brightness and other properties are entirely empirical, but by comparing measurable properties of distant supernovae to well defined 'empirical templates', developed from well catalogued nearby events, we can fill in the missing information.

One more general model describing the light curves of Ia supernovae is the SALT2 model (Guy, Astier, & Baumont, 2007), which can recreate typical light SN-Ia curves observed by various common telescope band-filters. In this model, the light curves and brightness of a supernova are parameterized by its stretch (i.e. rate of brightness evolution). The model only provides average light for a typical supernova, and doesn't account for the significant scatter observed in real measurements (M., R., J., & Et, 2014).

3 SUPERNOVA ANIMATION

One of the two goals of this project was to extend the universe-map animation by Hinton (Hinton, 2016) to display DES supernovae, with their appearances changing in time to represent the evolution of their light curves. The original animation program was written in python, using the open source packages ‘math, numpy’ and ‘matplotlib’ with the 3D axes package, while the animation made use of the SN-Cosmo package to simulate SN light curves.

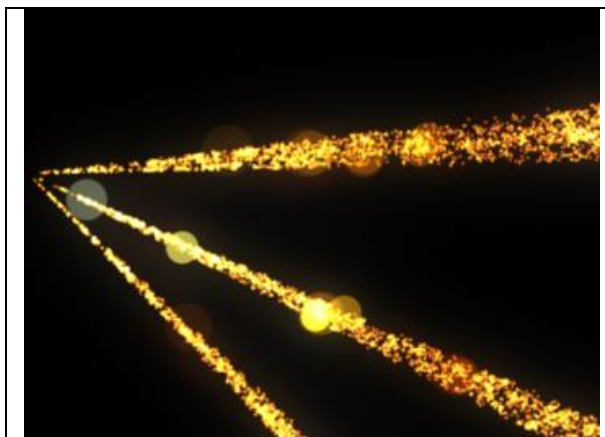


Fig 3.1-True Colour Animation Frame

3.1 SUPERNOVA SIMULATION

The OzDes supernovae data contains, for each supernova, the sky-position, redshift, magnitude, stretch, colour and date of peak brightness. With these properties, the SN-cosmo package (Barbary & Et, 2016) was used to simulate the light curves in python (fig 3.1.2), specifically retrieving the Bessel filter light curves in the infrared (I), red (R), visual (V), blue (B) and ultraviolet (U) filters (figure 3.1.1).

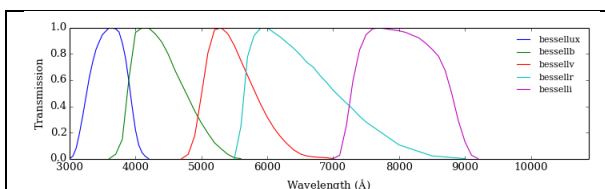


Fig 3.1.1-Bessel Band Passes (Barbary & Et, 2016)

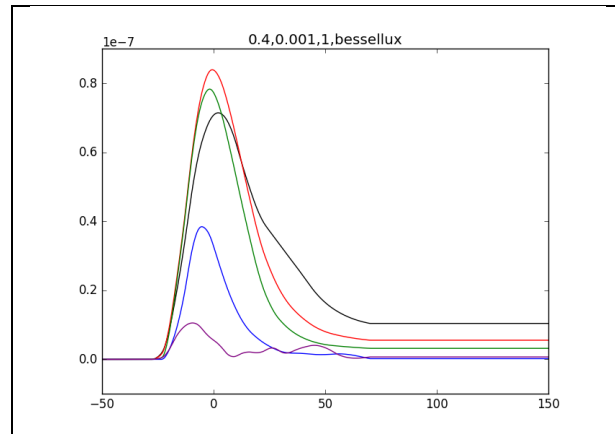


Fig 3.1.2 SN-Cosmo Light Curve

Supernovae were animated with a linear radial expansion, starting with zero size 25 rest-frame days before maximum light. The scale of this growth has no physical significance, and was chosen to make the supernovae clearly visible against the galaxy background without obscuring one another.

The brightness and opacity of the supernovae was set to be proportional to the total luminosity, as approximated from the RGB channels (see the false color scheme section) divided by square of radius, to give the appearance of a fading surface brightness:

$$Brightness \propto \frac{\sum(R, G, B)}{(t - t_{peak} + 25)^2}$$

The factor of proportionality was chosen so that the supernovae reach brightness close to one at their maximum.

The animation was written to be run both with and without time dilation and cosmological redshift, so that supernovae may appear as they do in their rest frame, or in our observation frame. When the animation is set to include redshift, expansion is slowed by factor of (1+z) to show time dilation, and the redshift/time dilation of the light curves is included in SALT2

model. If the animation does not include redshift, $z=0$ is input to the SALT2 model for all supernovae, and the time dilation factor is not used.

3.2 FRAME RENDERING

The animation code written by Hinton is set to import multiple surveys into a ‘visualiser’, which then produces a 3D scatter plot of these galaxy positions, and rasterizes this into a 2D image. Video animations are created by rendering multiple images in sequence, and then combining them with an additional video creation program.

To overcome limitations in python’s plotting software, Hinton renders the images additively to make galaxies appear as glowing clouds rather than opaque sheets of constant color. Python’s default rendering only adds the opacity ($\alpha \in [0,1]$) of overlapping points in a point series, maintaining their colour but increasing their brightness (figure 3.2.1):

$$\begin{pmatrix} R \\ G \\ B \end{pmatrix} = \begin{pmatrix} \min(R_i \cdot \sum \alpha_i, 255) \\ \min(G_i \cdot \sum \alpha_i, 255) \\ \min(B_i \cdot \sum \alpha_i, 255) \end{pmatrix}$$

black → coloured

Conversely, an additive scheme adds the channels RGB channels themselves, allowing the colour to change towards white as the brightest RGB channel caps out at 255 (figure 3.2.2). This gives a better visual gauge of point density.

$$\begin{pmatrix} R \\ G \\ B \end{pmatrix} = \begin{pmatrix} \min(\sum \alpha_i, 1) R_i \\ \min(\sum \alpha_i, 1) G_i \\ \min(\sum \alpha_i, 1) B_i \end{pmatrix}$$

black → coloured → white

Hinton’s animation does this by separating the large numbers of galaxy entries (several thousand) from the survey into ‘n’ layers (typically 20), rendering each layer as a single image, and then adding the RGB channels on top of one another before ‘clipping’ values above 255. One consequence of this is that there are no ‘black’ objects in the images, brightness and opacity are proportional. Gaussian blur is then applied to smooth the image out.

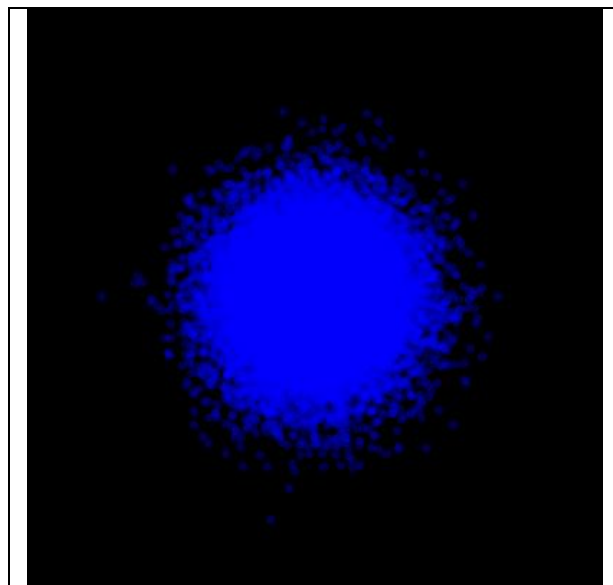


Fig 3.2.1-Python Default Rendering

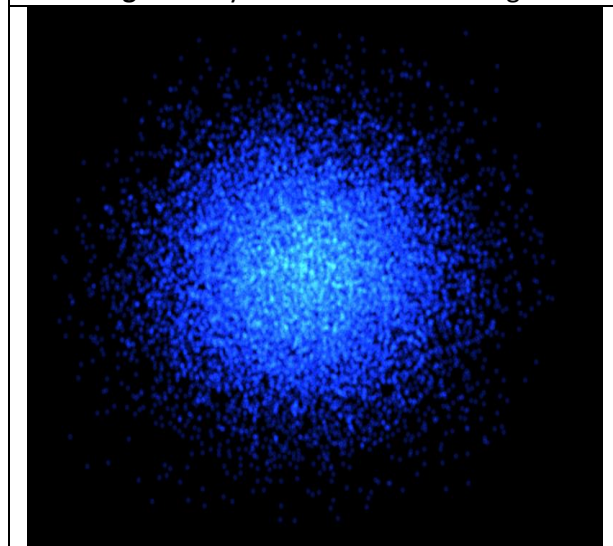


Fig 3.2.2-Additive Rendering (No Gaussian Blur)

For supernova animation, the code was extended to read the supernovae data as an additional survey class, containing information about the peak time, brightness, stretch and colour of each supernova in addition to the standard galaxy information of angular position and redshift. The visualiser was then altered to adjust the size and colour of each entry in the supernova survey based on the input time and entry properties. The light curves are calculated at the start of the animation, and each frame visualiser simply calls on the flux values required for each supernovae at the given time and frame.

3.3 FALSE COLOUR SCHEMES

The colour of the animated supernovae are defined by the light curves retrieved from SN-Cosmo, with different Bessel filters being mapped to the RGB channels of the dots that appear in the 3D scatterplot. The available filters are of varying band widths, and a true-colour scheme may not always communicate all desired information. As such, various false colour schemes were written into the animation code, in which the light curves of the five Bessel filters are mapped to the RGB channels in different proportions. For example, one false colour scheme (IVU2) has visual light appear green, infrared as red and ultraviolet as a dim blue:

$$\begin{aligned}
 R &\leftarrow F_I \\
 G &\leftarrow \frac{1}{3}(F_R + F_G + F_B) \\
 B &\leftarrow \frac{1}{2}F_U
 \end{aligned}$$

The channels are then scaled to 255 bit colour, with an additional ‘contrast’ parameter to intensify colour gradients. For example, the red channel is given by:

$$R \leftarrow 255 \left(\frac{R}{\max(R, G, B)} \right)^{contrast} \cdot \text{Brightness}$$

Where the brightness is as described in section 3.1. In total, I wrote five false colour schemes to complement the RGB true colour. The coefficients with which the filters are mapped to the RGB channels are listed in table 3.3.1.

Scheme	Channel	Filter				
		F _I	F _R	F _G	F _B	F _U
RGB	R	0	1	0	0	0
	G	0	0	1	0	0
	B	0	0	0	1	0
IVU1	R	1	0	0	0	0
	G	0	0	1	0	0
	B	0	0	0	0	1
IVU2	R	1	0	0	0	0
	G	0	1/3	1/3	1/3	0
	B	0	0	0	0	1/2
IVU3	R	1	1	1/2	0	0
	G	0	2/3	1/2	1	0
	B	0	0	1/2	1	1
RBSlide	R	1	1/2	1/2	1/2	0
	G	0	1/2	1/2	1/2	0
	B	0	1/2	1/2	1/2	1
RBSlide2	R	1	1	1/2	1/2	0
	G	0	1/2	1/2	1/2	0
	B	0	1/2	1/2	1	1

Table 3.3.1-Colour Scheme Coefficients

Examples of the different false colour schemes can be seen in appendix A.

4 WEAK GRAVITATIONAL LENSING MAP

The second component of this project was the use of the galaxy counts in the OzDes survey to develop a map of the estimated effects of weak gravitational lensing throughout the surveyed region. This section will outline the methods used to create this map, some investigated alternatives, and properties of the results they produced.

4.1 METHODS

The OzDes survey data used here is comprised of four contiguous ‘spokes’ covering different angular regions in the sky. To simplify computation and to avoid any effects from inherent differences between the regions, the survey was divided up and each spoke analyzed independently of the others.

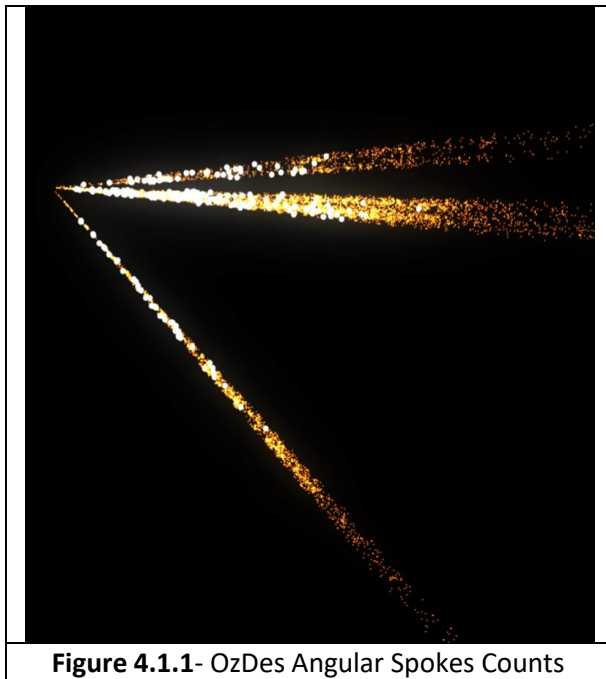


Figure 4.1.1- OzDes Angular Spokes Counts

Beyond redshifts of approximately $z=1$, the galaxy counts in each spoke drop sharply, indicating significant selection effects. To prevent these effects skewing the data, galaxies beyond $z=0.85$ were excluded. This upper limit was both conservative and practical, as this is also the highest redshift of the OzDes supernovae data used in the animation.

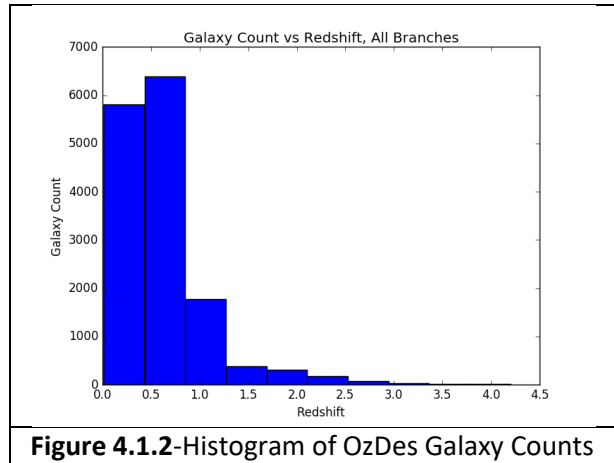


Figure 4.1.2- Histogram of OzDes Galaxy Counts

Table 4.1.1 gives the angular domain of each spoke, as well as their overall galaxy count.

Spoke	θ_{Min}	θ_{Max}	ϕ_{Min}	ϕ_{Max}	N gals, $z < 0.85$
1	0.11	0.19	-0.79	-0.73	2710
2	0.89	0.97	-0.53	-0.45	5044
3	0.58	0.66	-0.14	-0.06	3097
4	0.70	0.77	-0.04	0.02	1325

Table 4.1.1- OzDes Spoke Properties

4.1.1 MODEL

Though tracking the physical mass density on cosmological scales is extremely difficult, a crude estimate of the density fluctuation may be made by assuming that the mass within a region is proportional to the number of galaxies within that region:

$$\delta_\rho \equiv \frac{\rho}{\bar{\rho}} - 1$$

$$\delta_{\rho,ijk} \approx \frac{\left(\frac{N_{ijk}}{V_{ijk}}\right)}{\left(\frac{\bar{N}}{\bar{V}}\right)} - 1$$

Here, the ijk^{th} bin lies about angles i and j , and between redshifts k and $k-1$.

The means of counting galaxies, defining regions and determining the average density are described in sections 4.1.2 and 4.1.3. To form these regions, the survey was divided up by evenly spaced redshifts, ranging from 0 to 0.85, and the cosmological equations from section 2.1 discretized and numerically calculated:

$$a_k = \frac{1}{z_k + 1}$$

$$H_k = H_0 \sqrt{\Omega_\Lambda + \Omega_m(1 + z_k)^3}$$

$$\chi_k = c \sum_{k'=1}^k \left(\frac{1}{k'} + \frac{1}{H_{k'-1}} \right) \cdot \Delta z_{k'}$$

This allows the discrete form of the lensing magnification given in 2.2 to be calculated:

$$\delta m_k = \frac{15H_0^2 \Omega_m}{2 \ln|10| c^2} \sum_{k'=k}^k \frac{\delta_{k'} \chi_{k'}}{a_{k'}} \left(1 - \frac{\chi_{k'}}{\chi_k} \right) \Delta z_{k'}$$

Only coarse 0^{th} and 1^{st} order numerical integration methods are used here, as the density estimation itself is not precise enough to warrant any more complicated methods.

4.1.2 GALAXY COUNT METHOD

Calculation of the galaxy count density requires the galaxies to be counted within set volume bins. How the boundaries of these bins are defined has a strong effect on the results. In this project, the galaxy positions and bin boundaries were defined in polar coordinates of right-ascension (θ), declination (ϕ) and redshift (z).

The crudest method is to simply count the galaxies in exclusive rectangular domains, i.e. $N_{ijk} \equiv N \in [\theta_i, \theta_{i-1}] \ \& \ [\phi_j, \phi_{j-1}] \ \& \ [z_k, z_{k-1}]$

This is not particularly effective in that it introduces low count effects with increasing angular bin count (discussed in section 4.2.2) and also has a rotational asymmetry. A more appropriate method is to isolate the galaxies within a set angular circle (of angular radius 'R') of sky (tracing out a 'sight cone'), and then exclusively bin the enclosed galaxies by redshift.

$$N_{ijk} \equiv N \in \left[|(\theta - \theta_i)^2 - (\phi - \phi_j)^2| < R \right] \ \& \ [z_k, z_{k-1}]$$

As the cones can overlap, their size is independent of the number of allowable cones, allowing the density to be estimated at more points. Sight cones of various angular sizes (ranging from 6 to 18 arc-minute radii) were used for this report. The effects of changing this radius are discussed in 4.2.1.

A similar method of overlapping bins may also be employed for the redshifts, but is not investigated here .

4.1.3 DENSITY ESTIMATION

For δ to be found from the galaxy counts established in 4.1.2, the count density must be estimated, both the local and (ρ) and average ($\bar{\rho}$). As part of the development of the model, a number of ways to calculate both of these were investigated.

The most direct means of finding count density is to calculate the concave hull of the galaxies in z-space, numerically calculate its volume, and simply divide the total number through by this volume:

$$\bar{\rho} = \frac{N_{All}}{V_{CH}}$$

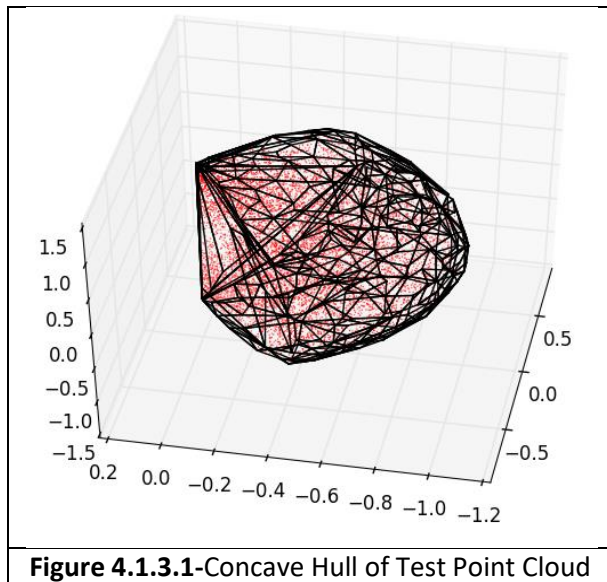


Figure 4.1.3.1-Concave Hull of Test Point Cloud

The main advantage of this method is that it uses the entirety of the survey data to acquire the most precise estimate of mean count density, though it is subject to a number of flaws. Irregular geometry and selection effects at the angular boundary of the survey can respectively increase the volume estimate and decrease the galaxy count, both serving to underestimate the mean density, making the angular interior appear overdense.

An alternative is to sample only well defined regions within the interior, either by taking many sight cones and averaging their result, or isolating a small number of larger regions, and finding their densities. The latter of these was used for this report, with the densities in 2-3 well defined regions being found and averaged for each spoke.

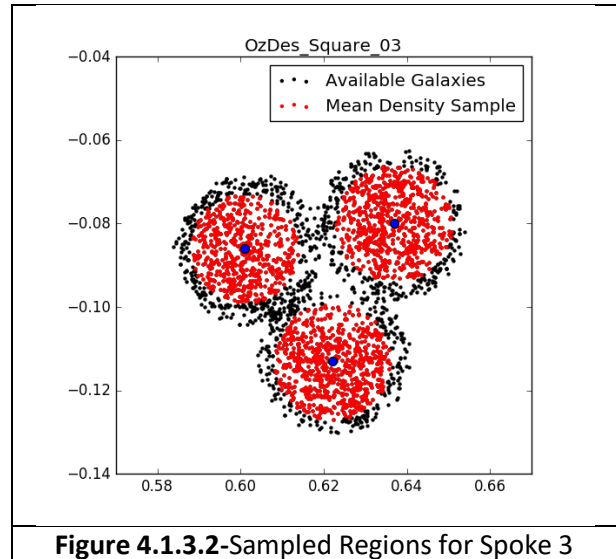


Figure 4.1.3.2-Sampled Regions for Spoke 3

Table 4.1.3.1 lists the locations, sizes and locations of these regions.

Spoke	Sample Region Property (Rad)		
	Ra	Dec	Radius
Spoke 1	0.135	-0.750	0.013
	0.165	-0.765	0.013
Spoke 2	0.947	-0.473	0.014
	0.919	-0.489	0.014
Spoke 3	0.947	-0.506	0.014
	0.601	-0.086	0.013
	0.637	-0.080	0.014
Spoke 4	0.622	-0.113	0.014
	0.718	-0.017	0.013
	0.747	0.000	0.013

Table 4.1.3.1-Density Sample Cones

Though this method is less general, requires manual selection of the sample regions and requires some survey data to be discarded, it is more robust, and avoids edge effects.

Another concern is that expansion and selection effects mean that the mean count density can change significantly with redshift. This can be countered by having $\bar{\rho}$ as a function of z , using the same method on concentric ‘shells’ of the survey instead of the entire domain. By only comparing bins to the average count density within their corresponding shell, expansion and z -dependent selection effects will cancel out.

This is particularly important for the OzDes survey, in which the density varies with z . Instead of number galaxy counts growing quadratically, as would be seen in the absence of such effects, each survey has an irregular distribution that rises and falls (fig 4.1.3.3)

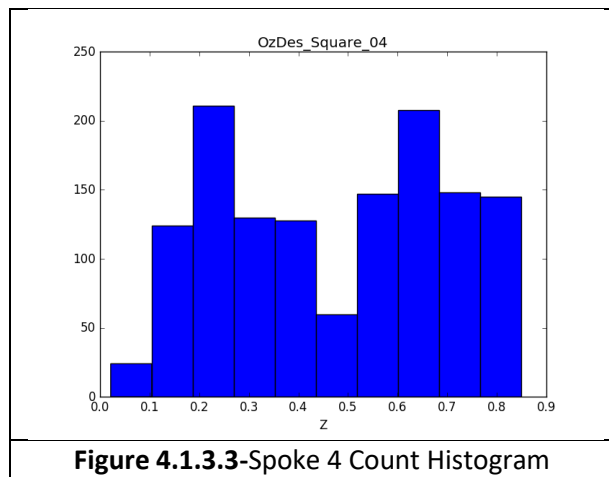


Figure 4.1.3.3-Spoke 4 Count Histogram

Table 4.1.3.2 shows the average count density for the 5 shells that the OzDes spokes were divided into, as found from the sampling regions in table 4.1.3.1.

Z_{Max}	Count Density ($10^6/z^3$)			
	Spoke 1	Spoke 2	Spoke 3	Spoke 4
0.17	67	204	66	22
0.34	22	41	21	4
0.51	8	8	5	4
0.68	6	6	6	2
0.85	3	3	3	0

Table 4.1.3.2-Spoke Z-Shell Count Densities

In models with a more rigorous modeling of cosmological expansion and selection effects, this z -shell method may later be replaced, instead using the whole survey for a more precise estimate of $\bar{\rho}$.

4.2 RESULTS

This section will outline the findings of the magnification map component of the project, both the recovered phenomena and how they are affected by altering the parameters of the binning model.

4.2.1 STRUCTURE & RESOLUTION

With a survey of limited galaxy counts, as with the OzDes data, precision of results is strongly dependant on the size of the bin regions, i.e. the number of redshift-bins and the angular size of the sight cones. If the bin regions are too large, the fine detail is lost and magnification effects are underestimated, and if they are too small, the captured galaxy counts become too small to accurately estimate the density fluctuations.

The later ‘count effect’ is of particular concern, as, in addition to decreasing precision, it introduces a bias towards overdensity. Consider a survey or z -shell of constant count density, with N points across volume V , the probability of finding ‘ n ’ points in volume ‘ v ’ is:

$$P(n \in v) = \left(\frac{v}{V}\right)^n \left(1 - \frac{v}{V}\right)^{N-n} \frac{N!}{n!(N-n)!}$$

If $\frac{v}{V} \approx 0.5$ and N is large, this forms a normal distribution about the value $n = \frac{v}{V}N$. However, as $\frac{v}{V} \rightarrow 0$, the distribution becomes right-skewed, an effect that becomes particularly apparent when the dispersion is high compared to the average, i.e. when $\frac{v}{V}N \approx 1$:

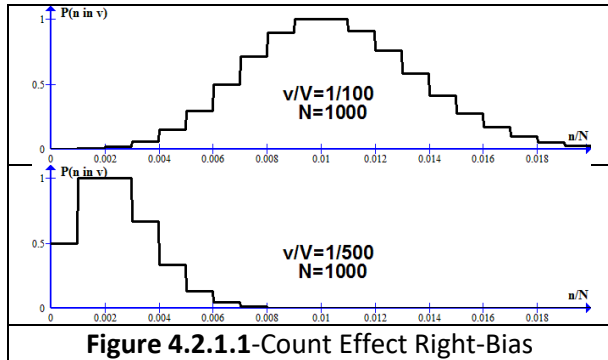


Figure 4.2.1.1-Count Effect Right-Bias

If the average density is based on a sample affected by this low-count effect, these bins appear to be over-dense on average. Fortunately, count effects are most prevalent in the smaller low-redshift bins, in which have the smallest effect on the magnification.

effects, we required the smallest bin to contain many points:

$$N_{Min} \approx \bar{\rho}V_{Min} \approx \frac{N_{All} \theta^2}{n_z^3 \Theta} \gg 1$$

This provides a useful baseline for determining the maximum resolution that a particular survey can support without becoming overwhelmed by count effects.

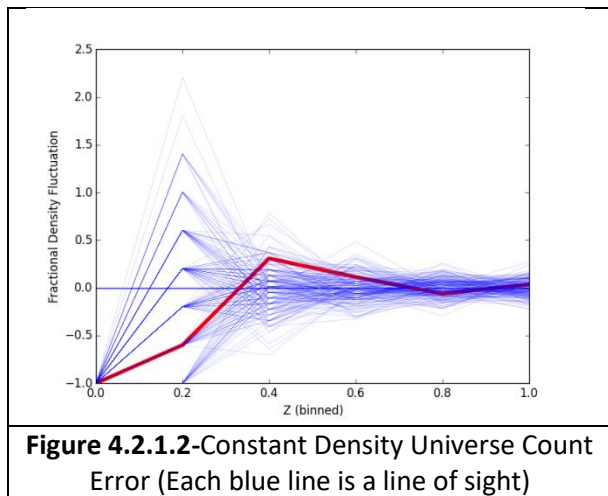


Figure 4.2.1.2-Constant Density Universe Count Error (Each blue line is a line of sight)

Consider a survey of N_{All} points evenly distributed through a cone split into n_z z-shells and of small angular radius Θ , containing a bin of angular radius θ . To avoid extreme count

Conversely, using too coarse a resolution can 'blur out' the structures that are of interest, making densities average out to the mean.

shell for spoke 1 for bins of angular radius 6, 12 and 18 arcminutes.

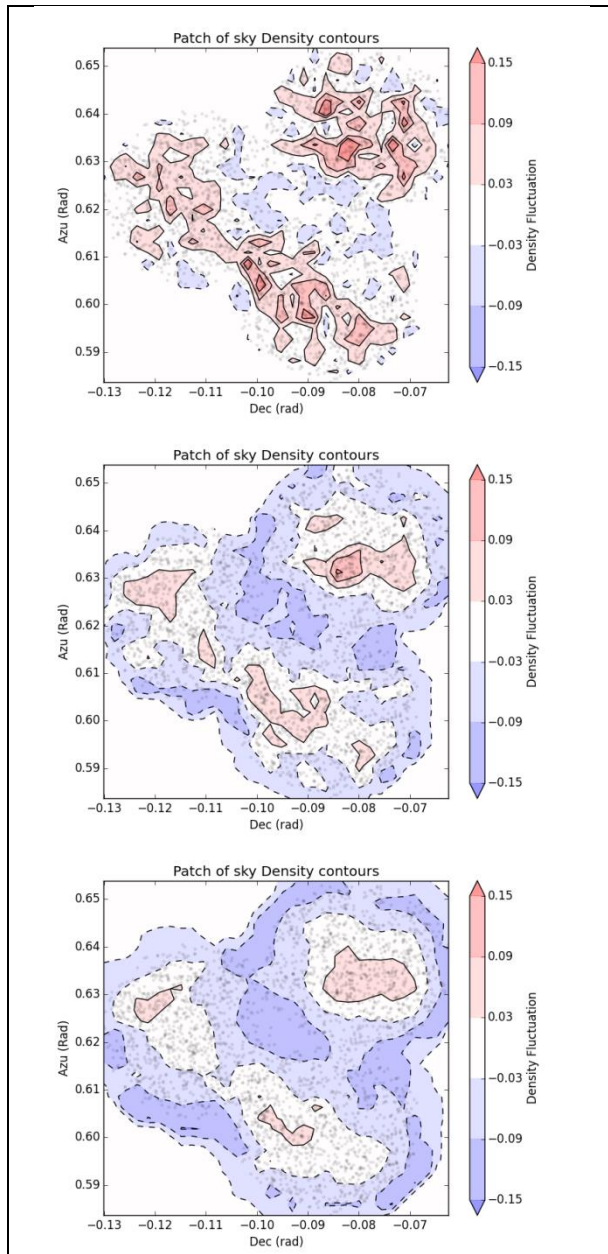


Figure 4.2.1.4-Spoke 3 Density Contours for Sight Cones of 6,12 and 18 arcminutes

See appendix B for the additional density plots.

The effects of changing the bin resolution can also be seen in the distribution of magnifications. Figure 4.2.1.5 shows the distributions of magnifications at the largest z-

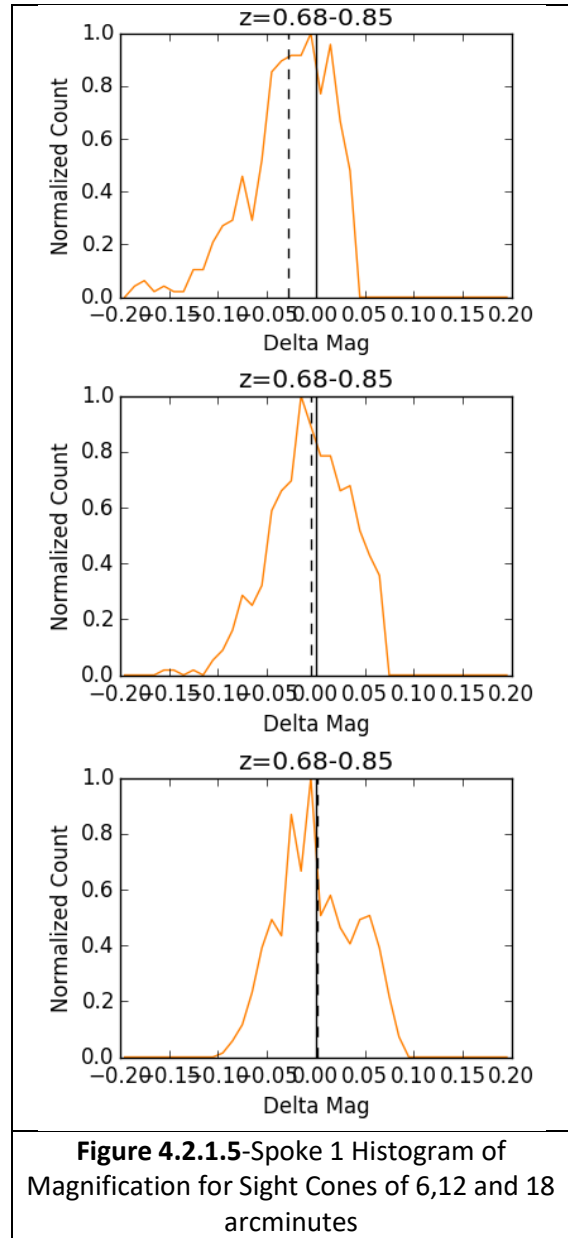


Figure 4.2.1.5-Spoke 1 Histogram of Magnification for Sight Cones of 6,12 and 18 arcminutes

It can be seen that fine resolution reproduces the magnifying tail, but also causes a bias in the average, while coarse resolution maintains the average, but also returns a more symmetrical distribution, not in keeping with the literature (Perlmutter & Schmidt, 2003).

A similar pattern is observed for the remaining 3 spokes, though the degree of the average-shift and symmetry loss vary. In spoke 3 (low mean density), the asymmetry is still very much present at coarse resolution, and in spoke 2 (high mean density) the average is reasonably consistent even at fine resolution. See appendix C for additional evolution diagrams.

4.2.2 MAGNITUDE & DISTRIBUTION

The results presented here are drawn from spoke 2, as it has the highest galaxy count, and is thus less subject to resolution artifacts, and a sight-cone radius of 9 arcminutes, as this is the finest resolution that doesn't produce distinct low-count effects. In figure 4.2.2.1, the typical magnification evolution can be seen: an increase in dispersion with the average remaining consistent at $\delta_m \approx 0$.

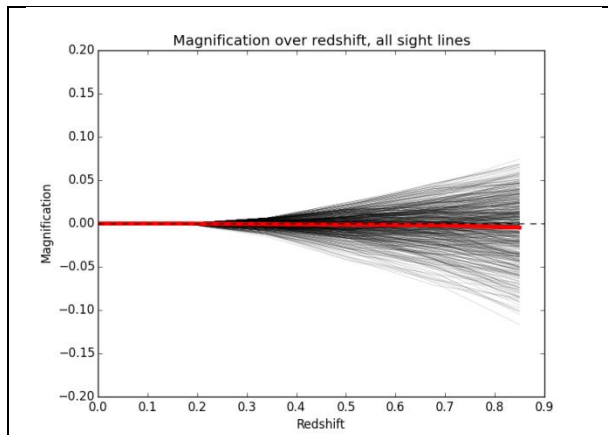


Figure 4.2.2.1-Spoke 2 Magnification Evolution (Each black line is a line of sight, away from the survey edges)

The asymmetry of the distribution becomes more apparent when the histogram of magnification is plotted for each z-shell (figure 4.2.2.2). Particularly at the higher z-bins, the peak probability is shifted above the maximum, and a tail is observed towards the negative.

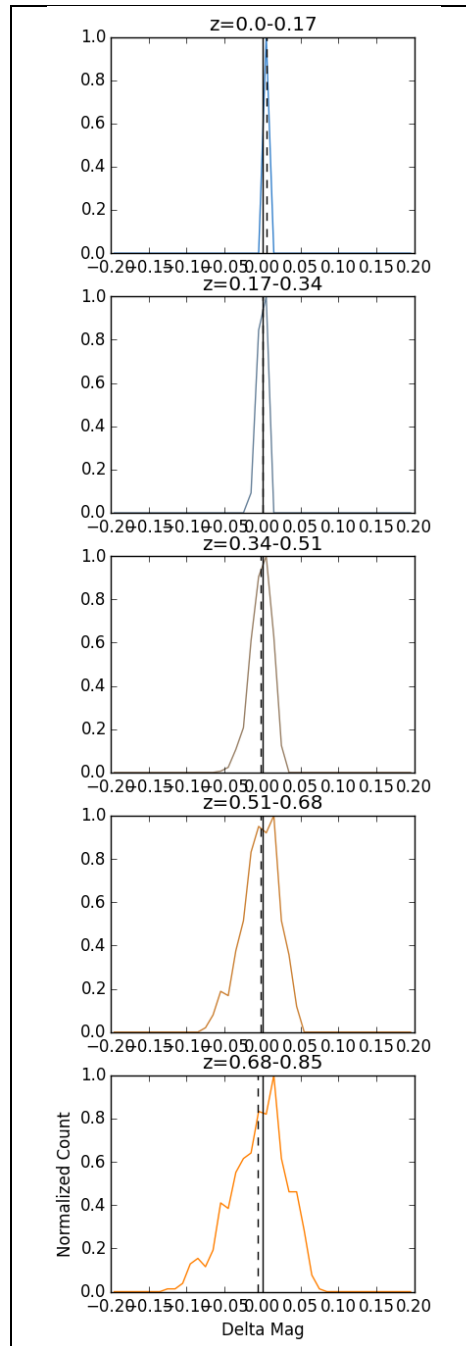


Figure 4.2.2.2-Histograms of δ_m , Spoke 2, 9 Arcmin

Though the asymmetry is noticeable, it is small. This stands in contrast to a low resolution (18 arcminute) analysis of the low-density spoke 4 (figure 4.2.2.3). In this instance, though the resolution is for more coarse and the average still 0, the asymmetric distribution of

magnification is far more distinct, particularly at high z (figure 4.2.2.4).

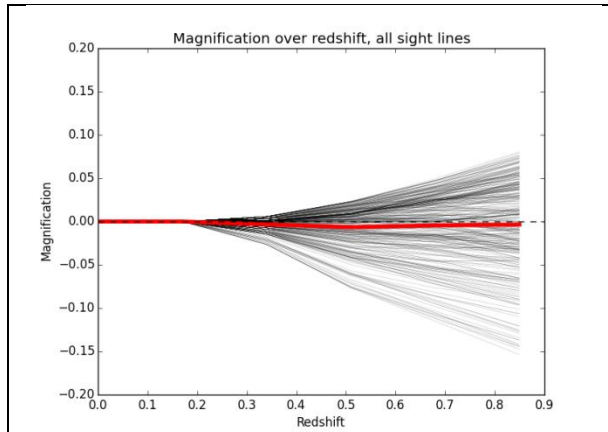


Figure 4.2.2.3-Spoke 4 Magnification Evolution

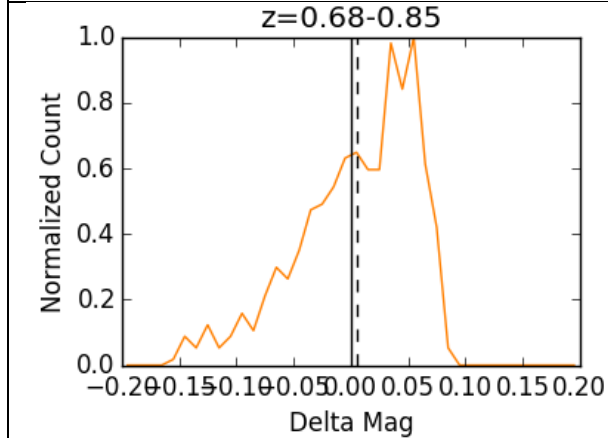


Figure 4.2.2.4-Spoke 2 High Z Magnification Distribution

It is interesting that, despite the coarse resolution of the spoke 4-18 arcminute instance removing finer overdense structures, as compared to spoke 2-9 arcminute instance (figure 4.2.2.5) it produces a stronger asymmetry of magnification.

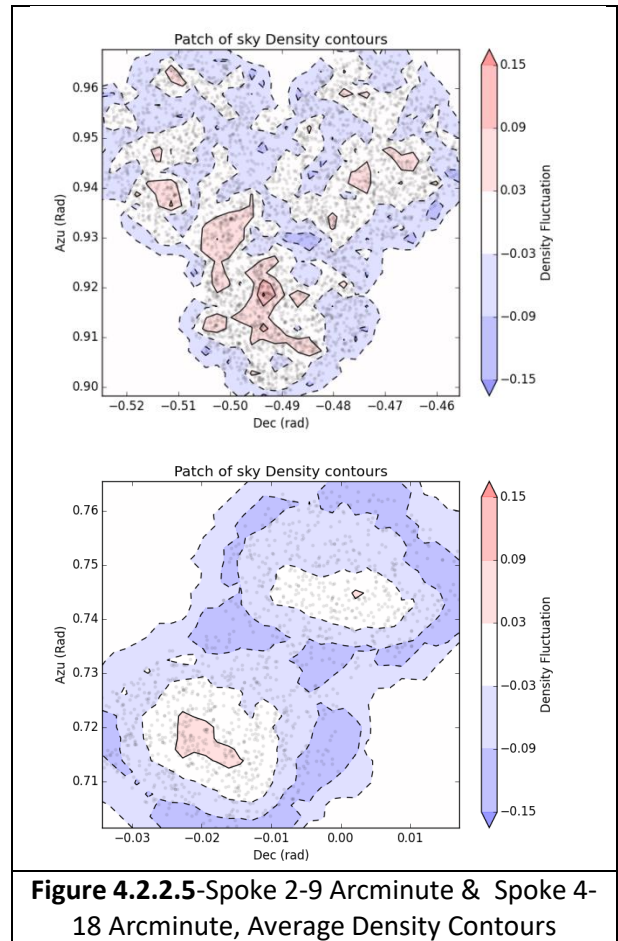


Figure 4.2.2.5-Spoke 2-9 Arcminute & Spoke 4-18 Arcminute, Average Density Contours

Given the absence of noticeable low count effects or an average demagnification, (figure 4.2.2.3), this is unlikely to be an artifact of spoke 2's low mean count density. Without further information, no conclusions can be drawn regarding the nature of this phenomenon.

5 CONCLUSION & RECOMMENDATIONS

5.1 SUPERNOVA VISUALIZATION

To summarize, the project's goal of extending Hinton's animation code to include a time-varying simulation of supernovae was a success, and accomplished all of the basic goals. Future work may seek to test the code on different surveys, in particular seeking to determine how the visual elements may need to be changed to accommodate more supernovae without overwhelming the animation. Work may also be done to include distorting effects, such as extinction or magnification, to the animation, so that it may be used to help provide an intuitive visualization of these biases and how they affect individual supernovae.

5.2 DENSITY MAP

Though the density map is practically functional, this project has not made any attempt to validate the model by checking for correlations with observed supernovae brightness. As the OzDes fields modeled already contain supernovae data, this checking of results would provide a measure of the model accuracy, and as well as the impact of any future improvements. Additionally, a simulation of cosmological structure may be a useful benchmark to compare density estimates to.

Some areas of interest for improving the model include a more robust counting method, such as overlapping redshift domains, changing the radial component from redshift to comoving distance or other alternatives, use of statistical methods to measure densities more precisely, and a more involved means of accounting for selection effects that accounts for both effects in redshift and viewing angle.

5.3 ADDITIONAL VISUALIZATIONS

This project has only focused on developing visualizations of supernovae and weak lensing, and there are many other biases that remain to be investigated. The OzDes data may well be used to look at effects such as peculiar velocity, gravitational redshift bias, or extinction, all from the assumption that mass density is proportional to galaxy count.

6 REFERENCES

Barbary, K., & E. A. (2016). *SN-Cosmo Documentation*. Retrieved from <https://sncosmo.readthedocs.io/en/v1.4.x/#>

Guy, J., Astier, P., & Baumont, S. (2007). SALT2: using distant supernovae to improve the use. *Astronomy & Astrophysics* .

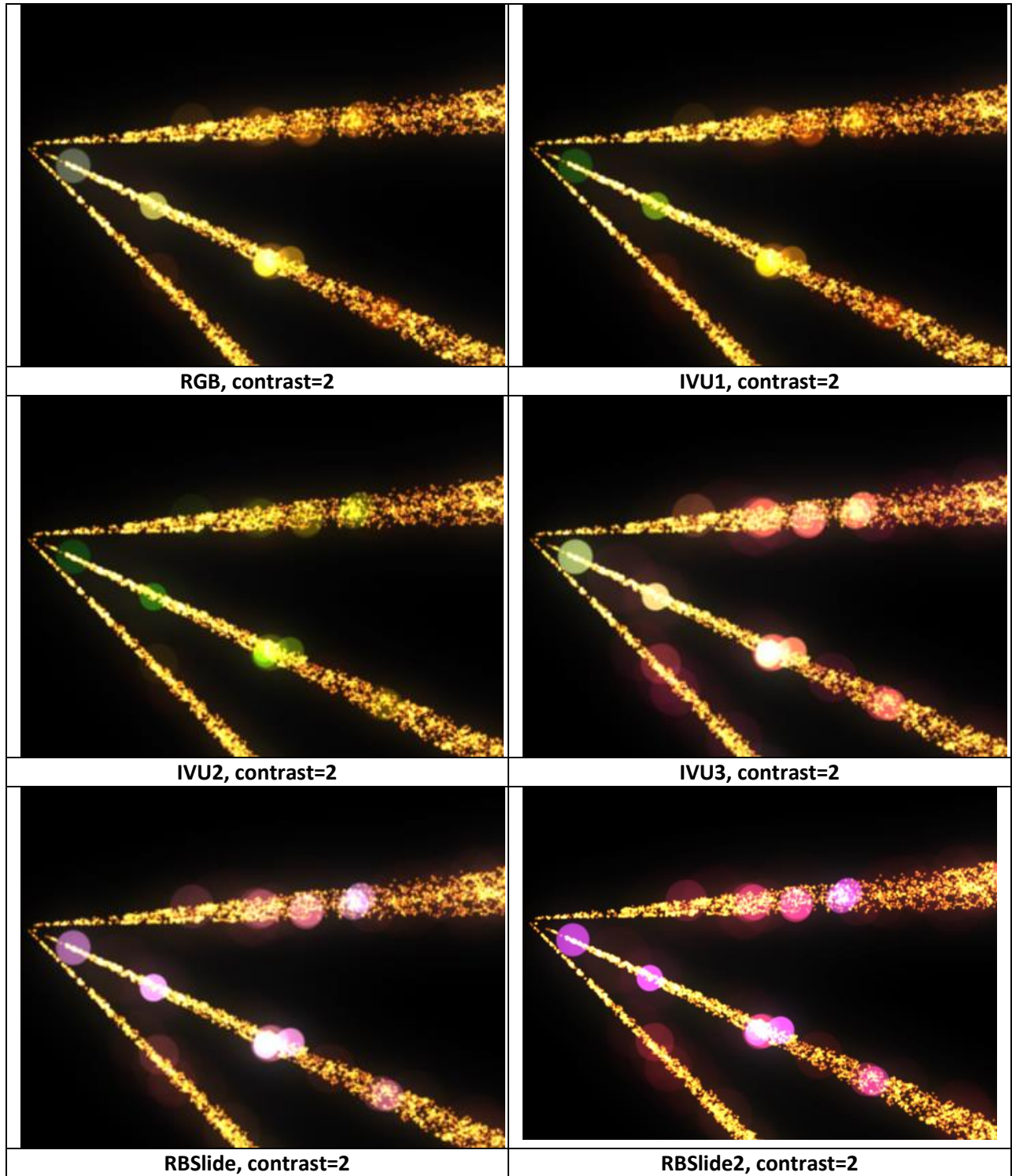
Hinton, S. (2016). *Additive Blending in Matplotlib*. Retrieved from <http://samreay.github.io/blog/2016/10/01/additive.html>

M., B., R., K., J., G., & E. A. (2014). Improved cosmological constraints from a joint analysis. *Astronomy & Physics* .

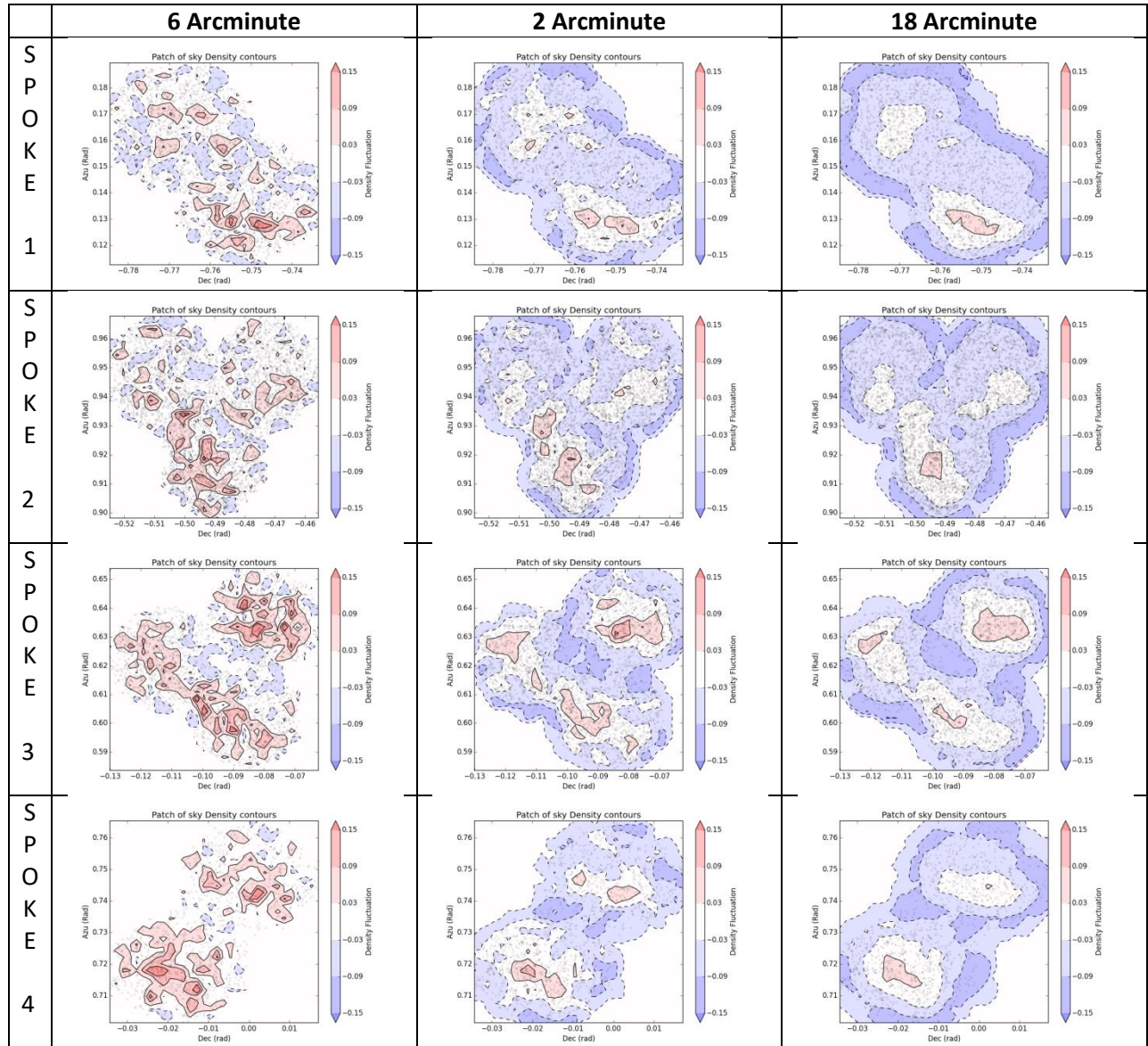
Perlmutter, S., & Schmidt, B. P. (2003). Measuring cosmology with Supernovae.

Taylor, M. (2016). *Mapping Magnification: Measuring mass density along the line-of-sight to*. Brisbane: Univeristy of Queensland Department of Science.

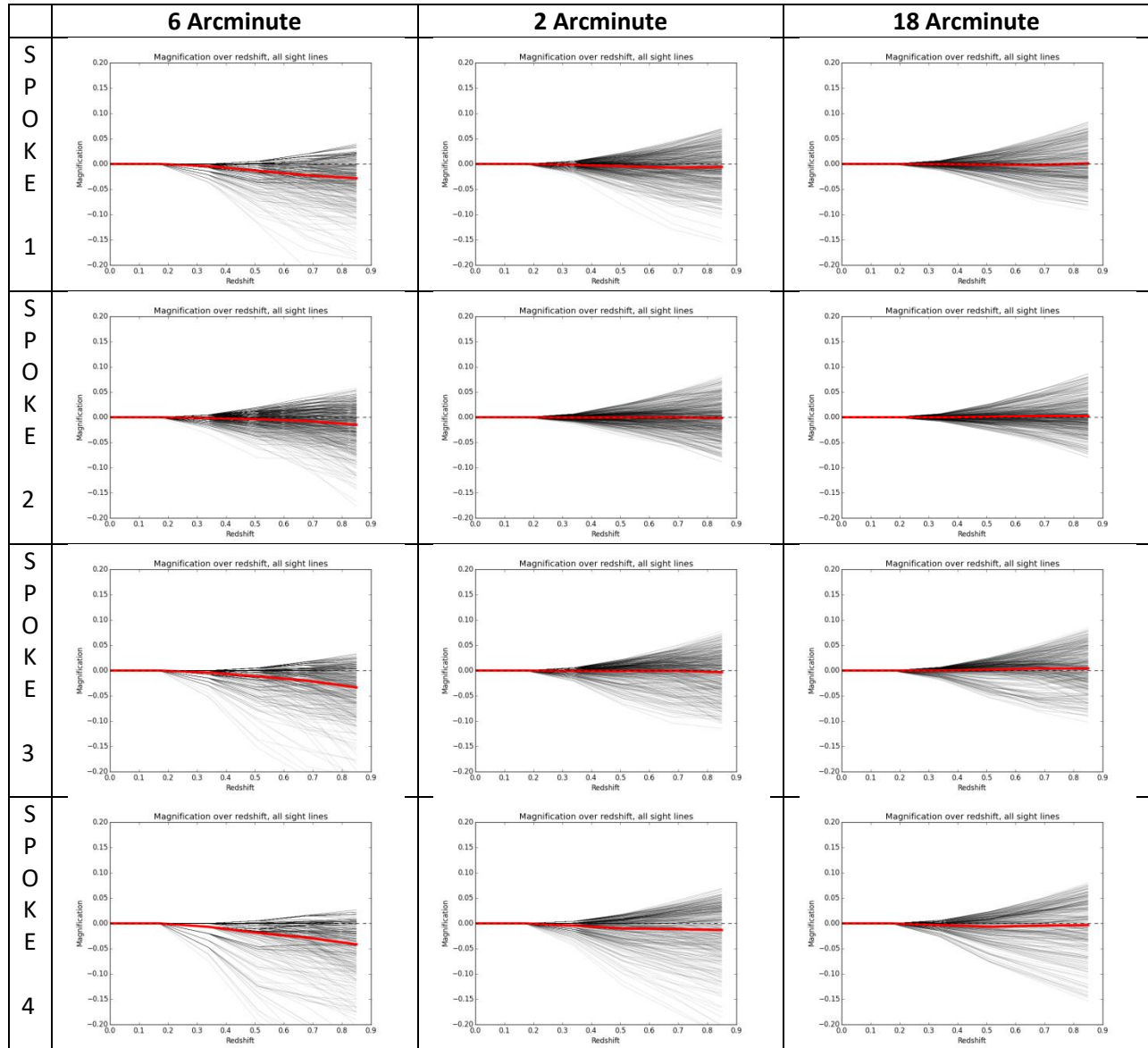
APPENDIX A- FALSE COLOUR SCHEMES



APPENDIX B: DENSITY MAPS



APPENDIX C: Z-EVOLUTION DIAGRAMS



APPENDIX D: MAGNIFICATION CONTOURS

